



HAL
open science

Global Ambipolar Potentials and Electric Fields at Mars Inferred From MAVEN Observations

Shaosui Xu, David L. Mitchell, Yingjuan Ma, Tristan Weber, David A. Brain,
Jasper Halekas, Suranga Ruhunusiri, Gina Dibraccio, Christian Mazelle

► **To cite this version:**

Shaosui Xu, David L. Mitchell, Yingjuan Ma, Tristan Weber, David A. Brain, et al.. Global Ambipolar Potentials and Electric Fields at Mars Inferred From MAVEN Observations. *Journal of Geophysical Research Space Physics*, 2021, 126, 10.1029/2021JA029764 . insu-03672337

HAL Id: insu-03672337

<https://insu.hal.science/insu-03672337>

Submitted on 30 Mar 2023

HAL is a multi-disciplinary open access archive for the deposit and dissemination of scientific research documents, whether they are published or not. The documents may come from teaching and research institutions in France or abroad, or from public or private research centers.

L'archive ouverte pluridisciplinaire **HAL**, est destinée au dépôt et à la diffusion de documents scientifiques de niveau recherche, publiés ou non, émanant des établissements d'enseignement et de recherche français ou étrangers, des laboratoires publics ou privés.

Copyright

JGR Space Physics

RESEARCH ARTICLE

10.1029/2021JA029764

Key Points:

- This work provides the first data-based characterization of global ambipolar electric fields at Mars (outside of the main ionosphere)
- We find averaged ambipolar potentials ranging from ~ -70 to $+100$ V and ambipolar electric fields of ~ 0.01 – 0.1 V/km
- MHD results show a good agreement with data-derived electric fields and also suggest the plasma source of these ambipolar electric fields

Supporting Information:

Supporting Information may be found in the online version of this article.

Correspondence to:

S. Xu,
shaosui.xu@ssl.berkeley.edu

Citation:

Xu, S., Mitchell, D. L., Ma, Y., Weber, T., Brain, D. A., Halekas, J., et al. (2021). Global ambipolar potentials and electric fields at Mars inferred from MAVEN observations. *Journal of Geophysical Research: Space Physics*, 126, e2021JA029764. <https://doi.org/10.1029/2021JA029764>

Received 7 JUL 2021
Accepted 3 DEC 2021

Global Ambipolar Potentials and Electric Fields at Mars Inferred From MAVEN Observations

Shaosui Xu¹ , David L. Mitchell¹ , Yingjuan Ma² , Tristan Weber^{3,4} , David A. Brain³ , Jasper Halekas⁵ , Suranga Ruhunusiri⁵ , Gina DiBraccio⁴ , and Christian Mazelle⁶ 

¹Space Sciences Laboratory, University of California, Berkeley, CA, USA, ²Department of Earth Planetary and Space Sciences, University of California, Los Angeles, CA, USA, ³Laboratory for Atmospheric and Space Physics, University of Colorado, Boulder, CO, USA, ⁴Goddard Space Flight Center, Greenbelt, MD, USA, ⁵Department of Physics and Astronomy, University of Iowa, Iowa City, IA, USA, ⁶IRAP, CNRS - University of Toulouse - UPS - CNES, Toulouse, France

Abstract The motion of charged particles is governed by electromagnetic forces at high altitudes at Mars and thus the characterization of electrostatic potential and electric fields is important for understanding ion escape at Mars. In this study, we utilize measurements from the Mars Atmosphere and Volatile Evolution mission to derive electrostatic potentials above the collisional atmosphere at Mars. We find averaged potentials to be up to ~ 100 V in the magnetosheath and down to ~ -70 V in the tail, with respect to the upstream. We then derive electric fields based on averaged potential maps, ranging ~ 0.01 – 0.1 V/km. These data-derived electric fields are in good agreement with ambipolar electric fields from a multi-fluid magnetohydrodynamic (MHD) model. MHD results also reveal that these large electric fields mainly originate from the electron pressure gradient in the magnetosheath and in the transition region from the hot solar wind flow to the cold ionospheric flow. This work provides the first data-based characterization of global ambipolar electric fields at Mars (outside of the main ionosphere).

Plain Language Summary The motion of charged particles is governed by electric and magnetic force at high altitudes at Mars and thus the characterization of electric fields is important for understanding ion escape, a form of atmospheric escape, at Mars. In this study, we utilize measurements from the Mars Atmosphere and Volatile Evolution mission to derive electric fields at high altitudes, which occur at density and/or temperature gradients in a collisionless plasma to maintain charge neutrality with highly mobile electrons and much slower moving ions. These data-derived electric fields are in good agreement with electric fields from a magnetohydrodynamic model. Model results also reveal the plasma source of these electric fields. Our characterization of these electric fields provides a better understanding of the interaction between Mars and the Sun and, to a large extent, Mars' atmospheric escape.

1. Introduction

Ion escape as an important atmospheric escape channel at Mars has been one of the main focuses of the Mars atmospheric community (e.g., Jakosky et al., 2018). Important forces that impact ion motions have been investigated with observations as well as simulations. For example, Halekas, Brain, et al. (2017) and Ma et al. (2019) provide a detailed characterization of the ion pressure gradient and $\mathbf{J} \times \mathbf{B}$ forces with Mars Atmosphere and Volatile Evolution (MAVEN) data and the global magnetohydrodynamic (MHD) simulations, respectively. The motional electric field, $-\mathbf{U} \times \mathbf{B}$, has long been proven at Mars to be important to drive the ion plume, an important channel for ion escape (e.g., Dong et al., 2015, 2017; Liemohn et al., 2014). Ambipolar electric fields arising from the electron pressure gradient (∇P_e) in the ionosphere provide an important initial acceleration for ions to escape. Previous studies determine this electric field with MAVEN data to be on the order of 10^{-3} V/km at Mars, maximizing at 200–300 km altitude and near the ion exobase, and a resulting integrated potential drop of $< \sim 1$ V in the ionosphere, (e.g., Akbari, Andersson, Peterson, et al., 2019; Collinson et al., 2015, 2019; Ergun et al., 2016; Xu et al., 2018). Studies have shown that correctly capturing ambipolar electric fields significantly increases the ion escape (e.g., Brecht et al., 2016; Ergun et al., 2016; Ma et al., 2019; Modolo et al., 2016). Meanwhile, studies have shown that various wave forms exist at Mars (e.g., Fowler et al., 2020; Harada et al., 2016), some of which could cause significant ion heating and provide another important source for ion initial acceleration (e.g., Fowler et al., 2018).

Ambipolar electric fields resulting from ∇P_e (because of electrons' higher mobility than ions) also exist outside of the main ionosphere. The cross-shock electrostatic potential in the de Hoffman Teller frame arises from the electron pressure gradient across the shock. Electrons in the sheath are energized across the shock, which in turn can be used to infer the cross-shock electrostatic potentials (e.g., Schwartz et al., 2019; Xu et al., 2021). Furthermore, Horaites et al. (2021) analyze electron energization separately for parallel and antiparallel directions, which suggests electric fields, likely ambipolar in nature, to exist within the sheath. In this study, we apply the approach used in Xu et al. (2021) and Horaites et al. (2021) to all the plasma regimes sampled by the MAVEN spacecraft (but above the main ionosphere) to provide the first data-based global characterization of these electric fields within the near-Mars plasma environment.

The characterization of these electric fields is also important for understanding solar wind electron precipitation onto the Mars nightside atmosphere, which is one of the main sources maintaining the nightside ionosphere (e.g., Adams et al., 2018; Cui et al., 2019; Fillingim et al., 2007; Lillis & Brain, 2013; Lillis, Mitchell, et al., 2018; Shane et al., 2016; Xu, Curry, et al., 2020; Xu, Mitchell, et al., 2016). Mitchell et al. (2001) invoked the existence of a wake potential to explain the much lower solar wind electron fluxes observed on Mars' nightside by the Mars Global Surveyor spacecraft. Similarly, nightside low-altitude solar wind electron fluxes measured by the Solar Wind Electron Analyzer (SWEA) instrument (Mitchell et al., 2016) onboard MAVEN are generally much lower than those in the pristine upstream. This study reveals the origin of the electrostatic potential that leads to the lowered precipitating solar wind electron flux.

It is worth mentioning that there are also more sporadic electric fields operating at Mars. For instance, large field-aligned electric fields associated with inverted-V electron signatures and discrete aurorae found at Earth's polar regions also operate at Mars, which results in an electrostatic potential drop of hundreds (sometimes a few thousands) of volts (e.g., Brain et al., 2006; Xu, Mitchell, et al., 2020). Poppe et al. (2021) utilize a 1.5-D particle-in-cell model to investigate the formation of a quasi-static, field-aligned potential within the Martian strong crustal magnetic cusp regions, arising from different magnetic reflection effects on the precipitating (isotropic) electrons and (beamed) ions, causing a $>2\times$ enhancement in local ion escape rate. There are also studies that utilize electron energy and/or pitch angle distributions to infer electrostatic potentials without specifying the cause/nature of the electric field (e.g., Akbari, Andersson, Fowler, & Mitchell, 2019; Collinson et al., 2016; Lillis, Halekas, et al., 2018).

In this study, we derive electrostatic potentials outside of the main ionosphere from the electron energization/de-energization by applying Liouville's theorem and comparing the distribution functions of upstream solar wind electrons and local electrons. We mainly use superthermal electron data measured by SWEA, combined with magnetic field data from the Magnetometer (MAG, Connerney et al., 2015). We also utilize MHD simulation results from Ma et al. (2019) to help interpret our data results. This paper is organized as follows: a case study is first presented in Section 2 to illustrate the methodology, followed by statistical results in Section 3 and the physical interpretation of these results in Section 4, and, lastly, discussions and conclusions are provided in Section 5.

2. Case Study: Methodology

To illustrate how the electrostatic potential is derived with MAVEN measurements, an orbit example on 2 April 2018 is shown in Figure 1. Magnetic fields are shown in the Mars-centered Solar Orbit (MSO) coordinate system, where X points from the center of Mars to the Sun, Z points to the north pole of Mars' elliptical orbit plane, and Y completes the right-handed system. In Figure 1, from right to left, the enhancements in both the magnetic field strength ($|B|$, panel b) and electron fluxes (panel d) suggest MAVEN crossed the bow shock at approximately 19:04 UT (universal time) at the flank. At $\sim 18:06$ UT, the slight enhancement in $|B|$, the reduced magnetic fluctuation, and the change in the magnetic direction indicate the crossing of the magnetic pileup boundary (MPB) or induced magnetic boundary (IMB). An obvious drop in measured electron fluxes occurred at 18:00 UT, which is caused by the spacecraft potential turning from positive to negative across the extreme ultraviolet (EUV) shadow (the extinction of EUV; Steckiewicz, 2017).

Similar to Xu et al. (2021), we obtain the field-aligned electron energization or de-energization by comparing the phase space density, or the distribution function (DF), of upstream solar wind electrons and local electrons measured by SWEA at a 2-s resolution (equivalent of ~ 8 km spatially), separated for parallel (approximated by pitch angles (PA) $0\text{--}30^\circ$) and antiparallel (approximated by PA $150\text{--}180^\circ$) directions. According to Liouville's

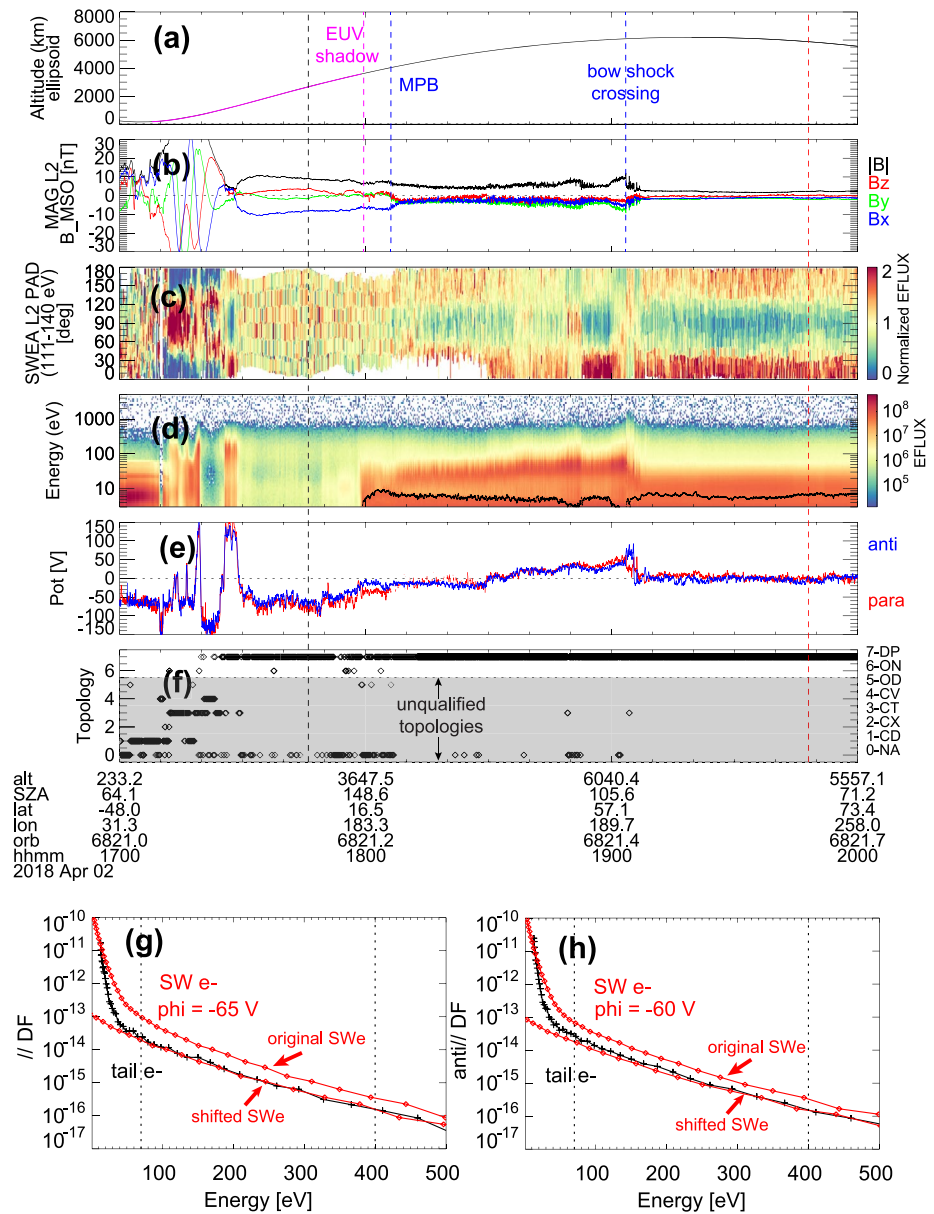


Figure 1. Time series of (a) altitude above the IAU Mars ellipsoid (Archinal et al., 2011), (b) magnetic field strength and components (nT) in Mars-centered Solar Orbit coordinates, (c) electron pitch angle distributions for 111–140 eV and (d) omnidirectional electron energy spectra measured by solar wind electron analyzer (SWEA), (e) derived potentials from parallel (red) and antiparallel (blue) electrons, (f) magnetic topology inferred from superthermal electron energy and angular distributions by SWEA. In (d), the black dotted line marks the positive spacecraft potential. Panels (g) and (h) show the comparison of the phase space density ($\text{cm}^{-3} (\text{km/s})^{-3}$) of upstream solar wind (SW) electrons and tail electrons, as well as the shifted SW electrons by -65 eV and -60 eV, for parallel (PA $0\text{--}45^\circ$) and antiparallel (PA $135\text{--}180^\circ$) directions, respectively, taken at times marked by the black and red vertical lines in the timeseries plot.

theorem, for field-aligned electrons, the energy change between the two DFs is the electron energization or de-energization (only using “energization” hereafter for simplicity) by electrostatic potential, for regions above the collisional atmosphere (~ 300 km altitude). In other words, we can infer the local potential relative to the upstream from the electron energization outside of the main ionosphere. All DFs are corrected for spacecraft potential. Spacecraft potential is derived from the current–voltage (I–V) measurements from the Langmuir Probe and Waves (LPW) instrument (Andersson et al., 2015) for positive spacecraft potentials and from the ion distributions from the SupraThermal And Thermal Ion Composition (STATIC) instrument (McFadden et al., 2015)

for negative spacecraft potentials (see detailed descriptions in the Methodology section of Xu et al., 2018). Both spacecraft potentials are available in the LPW and STATIC L2 data products.

An automated routine was designed and described in detail in Xu et al. (2021) to obtain local potentials relative to the upstream from parallel or anti-parallel electrons. We apply the same routine but an electron energy range of 70–300 eV is used instead for electron spectral comparison to accommodate electron deceleration in the tail, as described in detail in the Supporting Information S1. The potential results are shown in Figure 1e. To validate this automated procedure, an example of upstream solar wind electron DFs is shown as the red lines in panels (g) and (h), for parallel and antiparallel directions, respectively, taken at a time as marked by the vertical red dotted line. We then take example DFs in the Mars magnetotail at a time as marked by the vertical black dotted line and overlay them as the black lines in panels (g) and (h). We manually determine this potential by shifting the upstream DFs by certain energy to match the tail DFs, -65 eV and -60 eV here for parallel and antiparallel directions, respectively. We see a good agreement between the tail electron DFs and the shifted reference DFs for an energy range of ~ 40 – 500 eV, which indicates these tail electrons are solar wind electrons having experienced a total potential drop of ~ -60 V (negative sign = decelerating electrons). The mismatch at low energies is likely caused by electrons going through cross-shock acceleration first before being decelerated, which sometimes changes the spectral shape at low energies (Xu et al., 2021). Our automated routine gives a local potential of -70 V and -60 V from parallel and antiparallel electrons, respectively, as shown in panel (e), agreeing well with manually inferred local potentials.

Ideally, we should infer the same local potential from parallel and antiparallel electrons, which is mostly true for our case study (panel (e)). When these two potentials do differ, local potentials should be more reliable based on electrons traveling from upstream to downstream. This is because we can reasonably assume the upstream solar wind electrons to be steady and the same whether the field lines are connected to the induced magnetosphere or not. For simplicity, we choose the direction where electrons are traveling Sunward by combining the information of B_{XMSO} and pitch angles. More specifically, the parallel direction is chosen for $B_{XMSO} > 0$ and the antiparallel direction for $B_{XMSO} < 0$. We note that this approach might be problematic near the shock if electrons crossing the shock from downstream to upstream are selected and the reference solar wind electron distribution is taken on a field line unconnected to the bow shock, which occurs occasionally. However, the cross-shock potential has been well characterized by Xu et al. (2021) and is not the main focus of this study.

Another complication of generalizing the method used by Xu et al. (2021) to other plasma regimes is the possibility of comparing solar wind electrons to ionospheric photoelectrons. To ensure that we are comparing only solar wind-origin electrons, we utilize the topology database based on the technique provided by Xu et al. (2019), which can differentiate up to seven types of magnetic topologies, as indicated by Figure 1f. Topologies numbered 1–4 are different types of closed magnetic topologies, Topology 5 is open magnetic fields connected to the day-side ionosphere, Topology 6 is open magnetic fields connected to the nightside atmosphere (“open-to-night”), and Topology 7 is draped magnetic fields connected back to the solar wind on both ends. We limit our results to only Topologies 6 and 7, that is, “open-to-night” and draped, on both of which solar wind electrons are uncontaminated by ionospheric photoelectrons. Sunward electrons also ensure that we select only the precipitating electrons, rather than the back-scattered electrons, in the tail. Additionally, we define and calculate a relative error to select cases where DFs of upstream and local electrons agree well (see more details in the Supporting Information S1).

Our methodology requires approximations and assumptions. First, we approximate purely field-aligned electrons with PA 0 – 30° or 150 – 180° (limited by SWEA’s intrinsic angular resolution of 22.5°), which minimizes but does not eliminate the magnetic focusing effect. Second, our use of Liouville’s theorem carries the implicit assumption that micro instabilities (i.e., wave-particle interactions) do not significantly alter the DF, because of which we only select cases with similar DFs of upstream and local electrons. We expect wave-particle interactions to preferentially change electron DFs in certain energies (rather than across all energies) such that the resulting DFs significantly depart from pristine upstream solar wind electron DFs. As demonstrated in Horaites et al. (2021), Liouville’s theorem works well at higher energies, even in the magnetosheath where wave activity is more intense than anywhere else in the Mars space environment. Note especially the agreement of the field-aligned parts of the DF when Liouville mapping in energy only (Figure 6 of Horaites et al., 2021). This agreement, even for a strongly anisotropic pitch angle distribution, demonstrates the validity of our approach. Lastly, we expect an insignificant

change in electron DFs from collisions with ions and/or neutrals above ~ 300 km altitude where superthermal electrons' transport time scale is much shorter than that of collisions (e.g., Xu, Liemohn, et al., 2016).

For our case study, as $B_{XMSO} < 0$ for most of the tail passing from 17:30 UT to 19:00 UT (Figure 1b), the antiparallel direction is more reliable. Potentials in panel (e) are near 0 outside of the bow shock, turn positive just downstream of the shock because of the cross-shock potential acceleration (e.g., Schwartz et al., 2019; Xu et al., 2021), mostly remain positive in the sheath, become significantly negative values across MPB at 18:06 UT, and keep dropping down to roughly -60 V in the tail. A large “positive” potential occurred at 17:24–17:30 UT, right at a current sheet crossing. This acceleration of electrons might be a result of a possible magnetic reconnection near this current sheet (Harada et al., 2020) and is likely caused by heating/acceleration by other (non-adiabatic) processes rather than electrostatic potentials.

3. Statistical Results of Potentials and Electric Fields

Now that we have established the validity of our methodology, we apply this procedure to all the available MAVEN data from 1 December 2014–1 April 2020 and use the derived values to conduct statistical analyses. Note that our results are only valid above the collisional atmosphere (~ 300 km altitude, as marked by the dashed circles in the top two rows of Figure 2). For this analysis, we transform to the Mars-Solar Electric (MSE) coordinates, where X_E is opposite to the solar wind flow, Y_E is parallel to the component of the upstream interplanetary magnetic field (IMF) perpendicular to X_E , that is, $\mathbf{B}_{YMSO} + \mathbf{B}_{ZMSO}$, and Z_E completes the right-handed system. More specifically, when MAVEN samples the upstream, we use the measured magnetic vectors as the upstream IMF (Halekas, Ruhunusiri, et al., 2017; Halekas et al., 2015). Otherwise, we use a proxy for the upstream IMF provided by Ruhunusiri et al. (2018).

The left column of Figure 2 shows the inferred local potentials in three projections. Globally, both panels (a) and (b) shows a near-zero potential outside of the empirical bow shock, as expected. An averaged positive potential is found in the sheath, maximum near the sub-solar region and decreasing with increasing solar zenith angle, mainly because electrons are energized across the bow shock and the cross-shock potential is weaker in the flank (e.g., Xu et al., 2021). The values are lower than those in Xu et al. (2021) (an averaged peak potential of ~ 200 V). This is because results in Xu et al. (2021) are a collection of cross-shock potentials alone while our results here are averaging cross-shock potentials, potentials in the magnetosheath, and/or near-zero potentials in the upstream, due to the variation in shock locations. From the magnetosheath to the magnetotail, the local potential varies from positive to negative, most negative in the deep tail (down to ~ -70 V), right behind Mars. Panel (c) shows the tail cut of the potentials with a most-negative potential of ~ -70 V in the deep tail. We note that results within $1.1 R_M$ or below 340 km altitude (indicated by the dashed circles in the top two rows), where collisions are significant, are likely not valid.

With the maps of the averaged potentials (ϕ), we calculate two components of the electric field, not the full vector, in each plane as $E_{x'} = -[\phi(x', y') - \phi(x' - \Delta x', y')]/\Delta x'$, $E_{y'} = -[\phi(x', y') - \phi(x', y' - \Delta y')]/\Delta y'$, and $|E_c| = \sqrt{E_{x'}^2 + E_{y'}^2}$, where x' and y' are the two axes in each plane and $\Delta x' = \Delta y' = 0.1 R_M$ is used. In order to obtain coherent electric field patterns, we first smooth ϕ in Figures 2a–2c over three points (i.e., $0.3 R_M$) in each direction to minimize sharp variations in potentials and then calculate the electric field. Figures 2d–2f display the magnitude (color) and direction (arrow) of electric field components, $\mathbf{E}_{XZ} = \mathbf{E}_X + \mathbf{E}_Z$, $\mathbf{E}_{XY} = \mathbf{E}_X + \mathbf{E}_Y$, $\mathbf{E}_{YZ} = \mathbf{E}_Y + \mathbf{E}_Z$, respectively.

There are two major sets of electric fields in the sheath in Figures 2d–2e, outward near the bow shock and inward on the inner side of the sheath with a magnitude ranging ~ 0.03 – 0.1 V/km. Behind the terminator ($X_E < 0$) and below the MPB, we see an averaged electric field of >0.01 V/km, up to 0.03 – 0.05 V/km, which points toward the center of the tail and toward Mars. In Figure 2f, there are significant electric fields with a magnitude of ~ 0.03 V/km that occur near the optical shadow, mainly pointing toward the center, consistent with Figures 2d–2e.

4. Physical Interpretation

In this section, we discuss the origin of the potentials and electric fields inferred from MAVEN data shown above. The leading terms in the generalized Ohm's law give the following form for the electric field in collisionless regions:

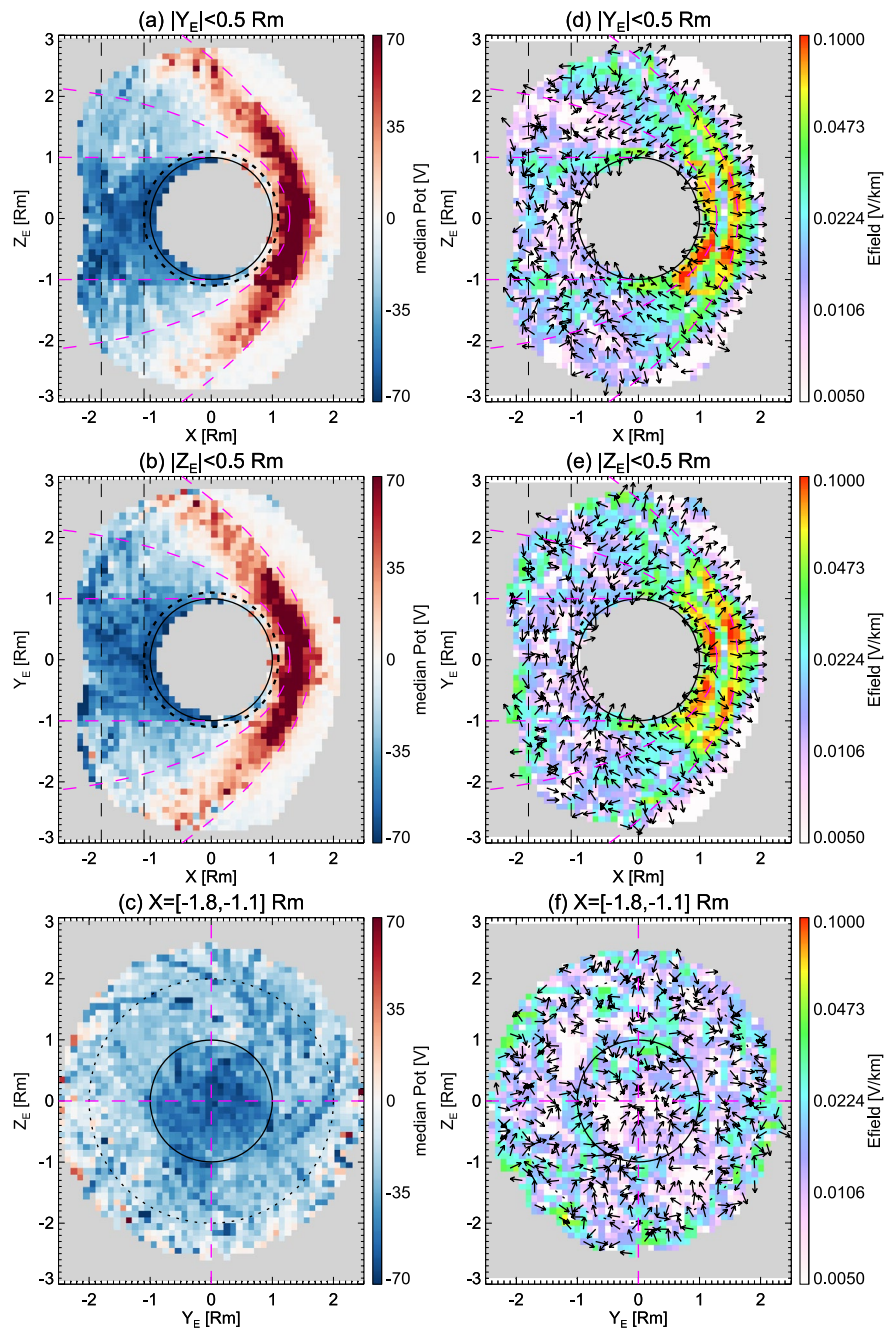


Figure 2. Mapping of local potentials (a)–(c) and electric fields (d)–(f) in the plane of $X_E - Z_E$ for $|Y_E| < 0.5 R_M$ (a), (d), $X_E - Y_E$ for $|Z_E| < 0.5 R_M$ (b), (e) and $Y_E - Z_E$ for $-1.8 R_M < X_E < -1.1 R_M$ (c), (f). The arrows in (d)–(f) show the direction of $\mathbf{E}_c/|\mathbf{E}_c|$ for $|\mathbf{E}_c| > 5 \times 10^{-3}$ V/km, where $|\mathbf{E}_c|$ is the corresponding electric field component in each plane. The magenta dashed lines in (a, b, d, e) are empirical fittings for the bow shock and the magnetic pileup boundary (Trotignon et al., 2006). The gray pixels are where there are less than 20 samples. Results within the dashed circle ($1.1 R_M$) in the top two rows, where collisions are significant, are likely not valid.

$$\mathbf{E} \approx -\frac{\nabla P_e}{en_e} + \frac{\mathbf{J} \times \mathbf{B}}{en_e} - \mathbf{U}_b \times \mathbf{B} \quad (1)$$

where n_e is the electron density, e is the fundamental charge, \mathbf{J} is the total current density, \mathbf{B} is the magnetic vector, and \mathbf{U}_b is the bulk flow velocity. The three terms on the right-hand side of Equation 1 correspond to the ambipolar electric field (\mathbf{E}_A), the Hall electric field (\mathbf{E}_H), and the motional electric field (\mathbf{E}_M).

Among the three electric fields, both \mathbf{E}_H and \mathbf{E}_M are in the direction always perpendicular to \mathbf{B} such that for gyrotopical electrons, these two terms do not change electrons' total energy but cause electrons to drift across magnetic fields. Our potentials are inferred from energy change in field-aligned electrons, whose drift across the field line is much smaller compared to their field-aligned motions, as also demonstrated in Horaites et al. (2021). That is, the ambipolar electric field is the only term that can change field-aligned electrons' total energy by its parallel component E_{\parallel} . However, as pointed out by Horaites et al. (2021), the ambipolar electric field can be expressed as a potential field, that is, $\mathbf{E}_A = -\nabla\phi$, if and only if $\nabla n_e \times \nabla T_e = 0$ (to give $\nabla \times \mathbf{E}_A = 0$), where T_e is the assumed isotropic electron temperature and ϕ the potential field. In the near-Mars plasma environment, this should be mostly satisfied as electrons are mostly isotropic and the change in electron density and temperature is either positively correlated (e.g., in the magnetosheath) or anti-correlated (e.g., in the ionosphere). In the case of $\mathbf{E}_A = -\nabla\phi$, the potential difference is independent of the integration path but only determined by the start and end points such that the full electric field \mathbf{E}_A (but not just E_{\parallel}) can be derived by taking the gradient of this potential field. Therefore, we interpret the local potentials and derived electric fields in Section 2 to be the full ambipolar potential and electric field \mathbf{E}_A . The fact that our derived electric fields would be almost perpendicular to typical draping IMFs in the sheath supports that this electric field is the full ambipolar electric field, rather than just the parallel component.

To further validate ∇P_e being the source of our derived potentials and electric fields, Figure 3 shows the electron pressure (a, b) and electric fields derived from the electron pressure gradient (c, d), that is, \mathbf{E}_A , from multi-fluid (MF) MHD simulations by Ma et al. (2019). This version of the MF-MHD model solves an additional electron pressure equation such that the electron temperature and the electron pressure force terms are solved self-consistently. Results in Figure 3 are from their simulations for Case 1 condition: a solar-maximum EUV intensity, strong crustal fields located on the dayside, a solar wind density and speed of 4 cm^{-3} and 400 km/s, and an IMF vector of $(-1.6, +2.5, 0.0)$ in MSO. As $B_{YMSO} > 0$ and $B_{ZMSO} = 0$, MSO is the same as MSE for this case.

Figures 3c and 3d show that the model predicts two sets of ambipolar electric fields near the bow shock, one pointing away from the shock and the other pointing inward in the magnetosheath. These two sets of electric fields are caused by the high electron pressure within the magnetosheath, as shown in Figures 3a and 3b. Closer to the planet, near MPB, there is another set of electric fields pointing toward the planet and the center of the tail behind Mars. This electric field is caused by the electron pressure gradient on the inner side of the magnetosheath on the dayside and also the switch from the high electron pressure of the shocked solar wind flow to the low electron pressure of the cold ionospheric flow in the flank (Figures 3a and 3b). It is informative to compare the magnitudes of three electric fields in Equation 1. From MHD, $|\mathbf{E}_A|$ is on the order of $\sim 0.1\text{--}1$ V/km near the bow shock and $\sim 0.01\text{--}0.1$ V/km near MPB, in comparison to $|\mathbf{E}_H| \sim 0.01\text{--}0.1$ V/km (not shown) near the bow shock and $|\mathbf{E}_M| \sim 0.1\text{--}1$ V/km near the MPB. Meanwhile, $|\mathbf{E}_M|$ is estimated to be on the order of ~ 1 V/km in the magnetosheath and the upstream by Horaites et al. (2021). In other words, the ambipolar electric field (\mathbf{E}_A) is comparable to the motional electric field (\mathbf{E}_M) and more important to decelerate and divert upstream solar wind flow than the Hall electric field (\mathbf{E}_H) near bow shock, but is a lesser force than the ion pressure gradient to be balanced with \mathbf{E}_H at MPB (e.g., Halekas, Brain, et al., 2017; Ma et al., 2019). In the meantime, \mathbf{E}_A is the only one of the three electric fields that has a field-aligned component that would significantly enhance or decrease electron fluxes via energization or de-energization.

These three sets of coherent ambipolar electric fields from MHD are in good agreement with MAVEN-data-derived electric fields shown in Figures 2d and 2e in spatial distributions, directions, and magnitudes. Admittedly, the data-derived electric fields are generally lower, roughly by a factor of 2. This is probably because (a) boundaries (such as the bow shock and MPB) where electric fields peak vary spatially throughout the mission so that the averaged electric field is smaller; (b) we smooth the potential field over $0.3 R_M$ in each direction to obtain coherent electric field patterns, which reduces the magnitude of the electric field as well.

Another significant discrepancy between the data and model is the electric field within the shadow, larger in Figures 2d and 2e than those in Figures 3c and 3d. In fact, the data-derived electric fields point toward Mars while the electron pressure distribution from MHD (Figures 3a and 3b) produce outward electric fields within the shadow (as shown in Figure S2 in Supporting Information S1). A few possible explanations: (a) the transition region from the hot solar wind electron flow to the cold ionospheric electron flow may vary spatially due to variations in upstream conditions, solar cycle, Mars seasons, and/or sub-solar longitudes such that the data-derived electric fields are distributed over a wider spatial region than model results; (b) we cannot derive too small electric fields from

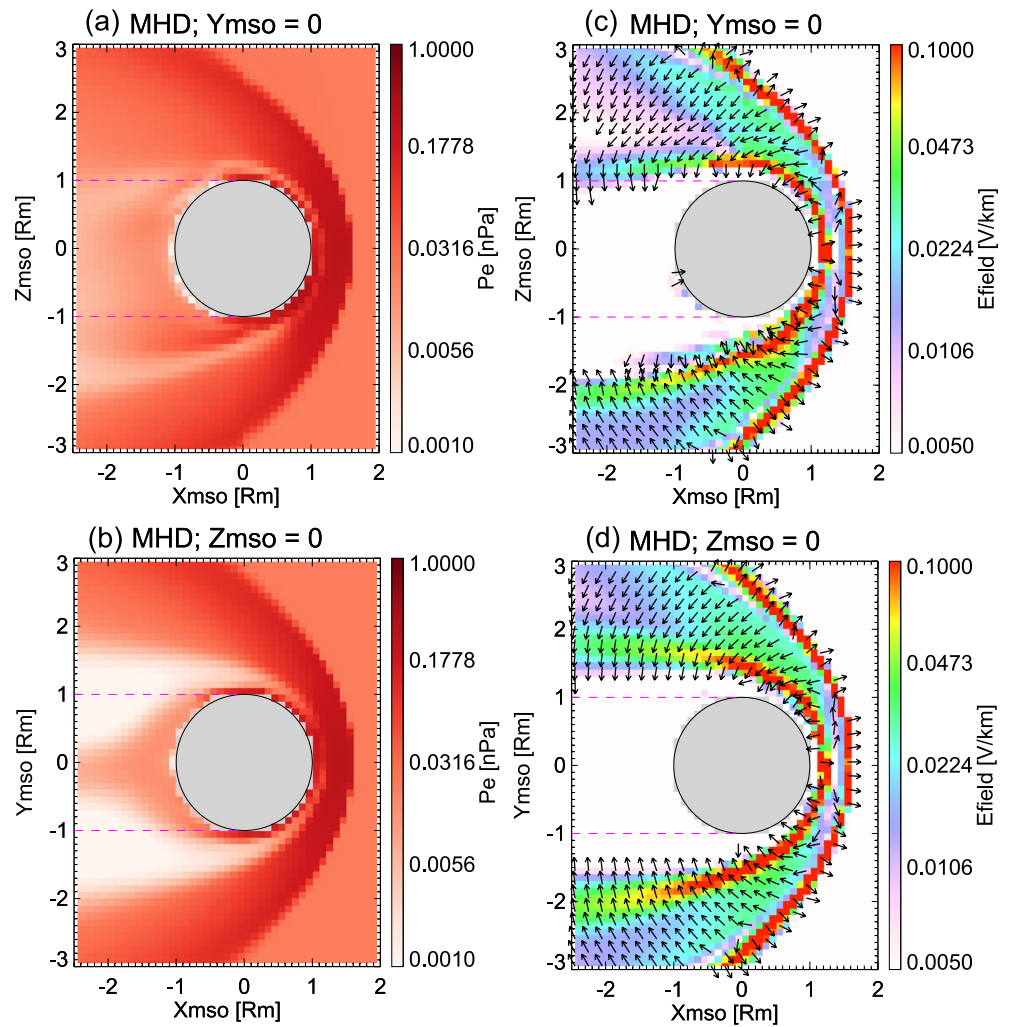


Figure 3. Electron pressure (a), (b) and electric fields derived from electron pressure gradient (c), (d) from magnetohydrodynamic simulations by Ma et al. (2019). (a) and (c) results in the $X_{MSO} - Z_{MSO}$ plane at $Y_{MSO} = 0$. (b) and (d) are results in the $X_{MSO} - Y_{MSO}$ plane at $Z_{MSO} = 0$. The arrows in (c)–(d) show the direction of $\mathbf{E}c/|\mathbf{E}c|$ for $|\mathbf{E}c| > 5 \times 10^{-3}$ V/km, where $|\mathbf{E}c|$ is the corresponding electric field component in each plane.

the data, but only those larger or comparable to the uncertainty. The uncertainty to data-derived electric fields can be estimated as $0.5\Delta E/\sqrt{NdL}$, where ΔE is the energy resolution of SWEA, N is the sample number in each bin, and dL is the spatial bin size. If we take $\Delta E = 16$ eV (for an energy channel of 100 eV), $N = 20$, and $dL = 0.1 R_M$, the uncertainty is approximately 5×10^{-3} V/km, which is why we omit plotting directions for electric fields smaller than this value in Figures 2 and 3.

5. Discussion and Conclusions

In this study, we apply Liouville's theorem and compare field-aligned electron distribution functions of upstream solar wind electrons and electrons downstream of the bow shock to infer electrostatic potentials relative to the upstream. With automated procedures, we obtain potentials from all available MAVEN/SWEA & MAG data for the time range of 01 December 2014–01 April 2020 (but only valid above the collisional atmosphere). We then statistically map this potential in the MSE frame and derive electric fields by calculating the gradient of averaged potential distributions. Our results show positive potentials with respect to the upstream solar wind, up to ~ 100 V, in the magnetosheath, which then turn negative near and below MPB, down to ~ -70 V in the Mars tail. Correspondingly, two sets of electric fields in the magnetosheath are obtained, pointing outward near the shock and inward on the inner side, with a magnitude ranging ~ 0.02 – 0.1 V/km. Additionally, there is a third set of electric

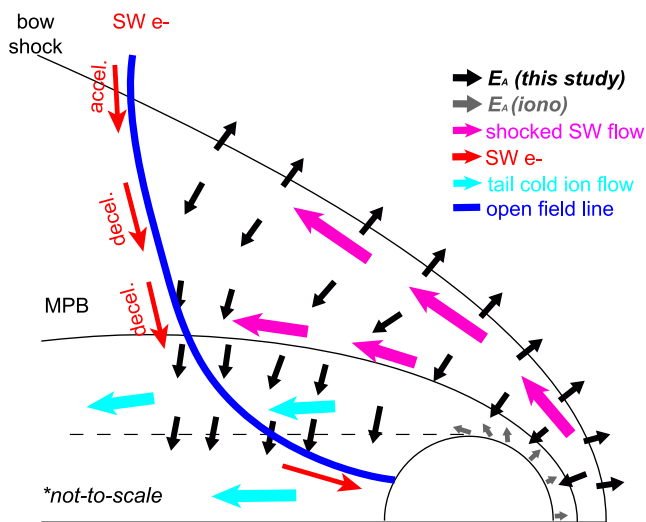


Figure 4. The schematic for ambipolar electric field and plasma flow directions at Mars (not to scale). The magnetic field line (blue) is for schematic purposes only. A more realistic field line would extend much farther down the tail before turning to match the unperturbed interplanetary magnetic field direction.

fields near and below MPB, generally directing toward the planet and the wake behind Mars, with a magnitude ranging $\sim 0.01\text{--}0.05$ V/km (excluding the dayside).

We interpret these data-derived potentials and electric fields to be ambipolar potential and electric fields originating from the electron pressure gradient from a theoretical point of view, that is, $\mathbf{E} = -\frac{\nabla P_e}{en_e}$. More specifically, ambipolar electric fields arise from electrons' higher mobility (lighter mass) than ions. We then compare these electric fields to ambipolar electric fields calculated from the MF-MHD simulations done by Ma et al. (2019). We find a good agreement between the data-derived and modeled ambipolar electric fields in terms of spatial distributions, directions, and magnitudes, apart from within the optical shadow where electric fields are smaller than the uncertainty in data results. Simulation results also suggest that these electric fields mainly originate from the electron pressure gradient in the magnetosheath as well as the transition from the hot solar wind electron flow to the cold ionospheric electron flow in the flank. This work provides the first data-based characterization of global ambipolar electric fields at Mars (outside of the main ionosphere).

Our work is also complementary to the characterization of near-Mars ambipolar potential and electric fields by Xu et al. (2018), which are mainly originated from the electron pressure gradient in the cold ionospheric flow as they focus on field lines connected to the dayside ionosphere. Their ambipolar electric fields are on the order of ~ 0.001 V/km, one to two orders of magnitude smaller than our results but are in a rough agreement with small electric fields near the planet in MHD results (as shown in Figure S2 in Supporting Information S1).

In contrast, the ambipolar potential and electric fields in our work mainly originate from the electron pressure gradient in the solar wind flow and/or the electron pressure difference between the shocked solar wind flow and the ionospheric flow. We note that ambipolar electric fields originating from cold ionospheric flow are comparable or smaller than our estimated uncertainty of 5×10^{-3} V/km such that our methodology cannot capture such small fields.

Our characterization of ambipolar electric fields outside of the main ionosphere at Mars has important implications for ion and electron motions. In terms of ion motions, the outward electric fields near the shock decelerate the upstream solar wind flow and the inward electric fields on the inner side tend to guide and divert the solar wind flow to the flank and down tail. The latter is also an additional force to be balanced with the $\mathbf{J} \times \mathbf{B}$ force near MPB. The inward electric fields near and below the MPB in the tail accelerate the shocked solar wind flow toward Mars and also inhibit ionospheric (mostly cold) ion outflow to diffuse outward but to mainly stream down tail. We summarize these aspects in a schematic shown in Figure 4.

In terms of electron precipitation onto the Mars nightside, solar wind electrons would first be accelerated by cross-shock potentials (e.g., Xu et al., 2021) and then decelerated by additional ambipolar electric fields in the flank, as shown in Figure 4 as well. The net effect is that solar wind electrons are usually significantly decelerated and low in flux, as observed by both MGS (e.g., Mitchell et al., 2001) and MAVEN when they reach the nightside atmosphere. In fact, magnetic field lines connected to the nightside would come from much further in the tail than illustrated where boundaries such as the bow shock and MPB are probably very diffusive. Thus, electrons should experience negligible cross-shock acceleration but mainly an accumulative deceleration by the ambipolar electric field before they reach the nightside atmosphere. This warrants caution not to directly use upstream solar wind electron distributions to estimate the impact of solar wind electron precipitation on the nightside atmosphere, such as the electron impact ionization and auroral emission.

Data Availability Statement

The MAVEN data used in this study are available through the Planetary Data System (<https://pds-ppi.igpp.ucla.edu/mission/MAVEN>).

Acknowledgments

This work was supported by the National Aeronautics and Space Administration (NASA) grant NNH10CC04C to the University of Colorado and by subcontract to Space Sciences Laboratory, University of California, Berkeley. The MAVEN project is supported by NASA through the Mars Exploration Program. S. Xu and D. L. Mitchell also acknowledge support from NASA's Mars Data Analysis Program, grant 80NSSC17K0455. Parts of this work for the observations obtained with the SWEA instrument are supported by the French Space Agency CNES (National Centre for Space Studies).

References

- Adams, D., Xu, S., Mitchell, D. L., Lillis, R. L., Fillingim, M., Andersson, L., et al. (2018). Using magnetic topology to probe the sources of Mars' nightside ionosphere. *Geophysical Research Letters*, *0*(ja). <https://doi.org/10.1029/2018GL080629>
- Akbari, H., Andersson, L., Fowler, C., & Mitchell, D. (2019). Spectral analysis of accelerated electron populations at Mars. *Journal of Geophysical Research: Space Physics*, *124*(10), 8056–8065. <https://doi.org/10.1029/2019ja026738>
- Akbari, H., Andersson, L., Peterson, W., Espley, J., Benna, M., & Ergun, R. (2019). Ambipolar electric field in the Martian ionosphere: MAVEN measurements. *Journal of Geophysical Research: Space Physics*, *124*(6), 4518–4524. <https://doi.org/10.1029/2018ja026325>
- Andersson, L., Ergun, R., Delory, G., Eriksson, A., Westfall, J., Reed, H., et al. (2015). The Langmuir probe and waves (LPW) instrument for MAVEN. *Space Science Reviews*, *195*(1–4), 173–198. <https://doi.org/10.1007/s11214-015-0194-3>
- Archinal, B. A., A'Hearn, M. F., Bowell, E., Conrad, A., Consolmagno, G. J., Courtin, R., et al. (2011). Report of the IAU working group on cartographic coordinates and rotational elements: 2009. *Celestial Mechanics and Dynamical Astronomy*, *109*(2), 101–135. <https://doi.org/10.1007/s10569-010-9320-4>
- Brain, D., Halekas, J., Peticolas, L., Lin, R., Luhmann, J., Mitchell, D., et al. (2006). On the origin of aurora on Mars. *Geophysical Research Letters*, *33*(1). <https://doi.org/10.1029/2005gl024782>
- Brecht, S. H., Ledvina, S. A., & Bougher, S. W. (2016). Ionospheric loss from mars as predicted by hybrid particle simulations. *Journal of Geophysical Research: Space Physics*, *121*(1010), 190–208. <https://doi.org/10.1002/2016ja022548>
- Collinson, G., Glocer, A., Xu, S., Mitchell, D., Frahm, R. A., Grebowsky, J., et al. (2019). Ionospheric ambipolar electric fields of Mars and Venus: Comparisons between theoretical predictions and direct observations of the electric potential drop. *Geophysical Research Letters*, *46*(3), 1168–1176. <https://doi.org/10.1029/2018gl080597>
- Collinson, G., Mitchell, D., Glocer, A., Grebowsky, J., Peterson, W., Connerney, J., et al. (2015). Electric mars: The first direct measurement of an upper limit for the Martian “polar wind” electric potential. *Geophysical Research Letters*, *42*(21), 9128–9134. <https://doi.org/10.1002/2015gl065084>
- Collinson, G., Mitchell, D., Xu, S., Glocer, A., Grebowsky, J., Hara, T., et al. (2016). Electric Mars: A large trans-terminator electric potential drop on closed magnetic field lines above Utopia Planitia. *Journal of Geophysical Research: Space Physics*. <https://doi.org/10.1002/2016ja023589>
- Connerney, J. E. P., Espley, J., Lawton, P., Murphy, S., Odom, J., Oliverson, R., & Sheppard, D. (2015). The MAVEN magnetic field investigation. *Space Science Reviews*, *195*(1–4), 257–291. <https://doi.org/10.1007/s11214-015-0169-4>
- Cui, J., Cao, Y.-T., Wu, X.-S., Xu, S.-S., Yelle, R. V., Stone, S., et al. (2019). Evaluating local ionization balance in the nightside Martian upper atmosphere during MAVEN Deep Dip campaigns. *The Astrophysical Journal*, *876*(1), L12. <https://doi.org/10.3847/2041-8213/ab1b34>
- Dong, Y., Fang, X., Brain, D., McFadden, J., Halekas, J., Connerney, J., et al. (2015). Strong plume fluxes at Mars observed by MAVEN: An important planetary ion escape channel. *Geophysical Research Letters*, *42*(21), 8942–8950. <https://doi.org/10.1002/2015gl065346>
- Dong, Y., Fang, X., Brain, D., McFadden, J., Halekas, J., Connerney, J., et al. (2017). Seasonal variability of Martian ion escape through the plume and tail from maven observations. *Journal of Geophysical Research: Space Physics*, *122*(4), 4009–4022. <https://doi.org/10.1002/2016ja023517>
- Ergun, R. E., Andersson, L. A., Fowler, C. M., Woodson, A. K., Weber, T. D., Delory, G. T., et al. (2016). Enhanced O₂⁺ loss at mars due to an ambipolar electric field from electron heating. *Journal of Geophysical Research: Space Physics*, *121*(5), 4668–4678. <https://doi.org/10.1002/2016ja022349>
- Fillingim, M. O., Peticolas, L. M., Lillis, R. J., Brain, D. A., Halekas, J. S., Mitchell, D. L., et al. (2007). Model calculations of electron precipitation induced ionization patches on the nightside of Mars. *Geophysical Research Letters*, *34*, 12101. <https://doi.org/10.1029/2007GL029986>
- Fowler, C. M., Agapitov, O. V., Xu, S., Mitchell, D. L., Andersson, L., Artemyev, A., et al. (2020). Localized heating of the Martian topside ionosphere through the combined effects of magnetic pumping by large-scale magnetosonic waves and pitch angle diffusion by whistler waves. *Geophysical Research Letters*, *47*(5), e2019GL086408. <https://doi.org/10.1029/2019GL086408>
- Fowler, C. M., Andersson, L., Ergun, R. E., Harada, Y., Hara, T., Collinson, G., et al. (2018). Maven observations of solar wind-driven magnetosonic waves heating the Martian dayside ionosphere. *Journal of Geophysical Research: Space Physics*, *123*(5), 4129–4149. <https://doi.org/10.1029/2018JA025208>
- Halekas, J., Brain, D., Luhmann, J., DiBraccio, G., Ruhunusiri, S., Harada, Y., et al. (2017). Flows, fields, and forces in the Mars-Solar wind interaction. *Journal of Geophysical Research: Space Physics*, *122*(11). <https://doi.org/10.1002/2017ja024772>
- Halekas, J., Ruhunusiri, S., Harada, Y., Collinson, G., Mitchell, D., Mazelle, C., et al. (2017). Structure, dynamics, and seasonal variability of the Mars-solar wind interaction: MAVEN Solar Wind Ion Analyzer in-flight performance and science results. *Journal of Geophysical Research: Space Physics*, *122*(1), 547–578. <https://doi.org/10.1002/2016ja023167>
- Halekas, J. S., Taylor, E. R., Dalton, G., Johnson, G., Curtis, D. W., McFadden, J. P., et al. (2015). The solar wind ion analyzer for MAVEN. *Space Science Reviews*, *195*(1–4), 125–151. <https://doi.org/10.1007/s11214-013-0029-z>
- Harada, Y., Andersson, L., Fowler, C. M., Mitchell, D. L., Halekas, J. S., Mazelle, C., et al. (2016). MAVEN observations of electron-induced whistler mode waves in the Martian magnetosphere. *Journal of Geophysical Research: Space Physics*, *121*(10), 9717–9731. <https://doi.org/10.1002/2016JA023194>
- Harada, Y., Halekas, J., Xu, S., DiBraccio, G., Ruhunusiri, S., Hara, T., et al. (2020). Ion jets within current sheets in the Martian magnetosphere. *Journal of Geophysical Research: Space Physics*, *125*(12), e2020JA028576. <https://doi.org/10.1029/2020ja028576>
- Horaites, K., Andersson, L., Schwartz, S. J., Xu, S., Mitchell, D. L., Mazelle, C., et al. (2021). Observations of energized electrons in the Martian magnetosheath. *Journal of Geophysical Research: Space Physics*, *126*(4), e2020JA028984. <https://doi.org/10.1029/2020ja028984>
- Jakosky, B., Brain, D., Chaffin, M., Curry, S., Deighan, J., Grebowsky, J., et al. (2018). Loss of the Martian atmosphere to space: Present-day loss rates determined from MAVEN observations and integrated loss through time. *Icarus*, *315*, 146–157. <https://doi.org/10.1016/j.icarus.2018.05.030>
- Liemohn, M. W., Johnson, B. C., Fränz, M., & Barabash, S. (2014). Mars express observations of high altitude planetary ion beams and their relation to the “energetic plume” loss channel. *Journal of Geophysical Research: Space Physics*, *119*(12), 9702–9713. <https://doi.org/10.1002/2014ja019994>
- Lillis, R. J., & Brain, D. A. (2013). Nightside electron precipitation at Mars: Geographic variability and dependence on solar wind conditions. *Journal of Geophysical Research: Space Physics*, *118*(6), 3546–3556. <https://doi.org/10.1002/jgra.50171>
- Lillis, R. J., Halekas, J., Fillingim, M., Poppe, A., Collinson, G., Brain, D. A., & Mitchell, D. (2018). Field-aligned electrostatic potentials above the Martian exobase from MGS electron reflectometry: Structure and variability. *Journal of Geophysical Research: Planets*, *123*(1), 67–92. <https://doi.org/10.1002/2017je005395>
- Lillis, R. J., Mitchell, D. L., Steckiewicz, M., Brain, D., Xu, S., Weber, T., et al. (2018). Ionizing electrons on the Martian nightside: Structure and variability. *Journal of Geophysical Research: Space Physics*, *123*(5), 4349–4363. <https://doi.org/10.1029/2017ja025151>

- Ma, Y. J., Dong, C. F., Toth, G., van der Holst, B., Nagy, A. F., Russell, C. T., et al. (2019). Importance of ambipolar electric field in driving ion loss from Mars: Results from a Multifluid MHD Model with the electron pressure equation included. *Journal of Geophysical Research: Space Physics*, *124*(11), 9040–9057. <https://doi.org/10.1029/2019JA027091>
- McFadden, J., Kortmann, O., Curtis, D., Dalton, G., Johnson, G., Abiad, R., et al. (2015). MAVEN suprathermal and thermal ion composition (STATIC) instrument. *Space Science Reviews*, *195*(1–4), 199–256. <https://doi.org/10.1007/s11214-015-0175-6>
- Mitchell, D. L., Lin, R. P., Mazelle, C., Rème, H., Cloutier, P. A., Connerney, J. E. P., et al. (2001). Probing Mars' crustal magnetic field and ionosphere with the MGS Electron Reflectometer. *Journal of Geophysical Research: Planets*, *106*(E10), 23419–23427. <https://doi.org/10.1029/2000je001435>
- Mitchell, D., Mazelle, C., Sauvaud, J.-A., Thocaven, J.-J., Rouzaud, J., Fedorov, A., et al. (2016). The MAVEN solar wind electron analyzer. *Space Science Reviews*, *200*(1–4), 495–528. <https://doi.org/10.1007/s11214-015-0232-1>
- Modolo, R., Hess, S., Mancini, M., Leblanc, F., Chaufray, J.-Y., Brain, D., et al. (2016). Mars-solar wind interaction: Lathys, an improved parallel 3-d multispecies hybrid model. *Journal of Geophysical Research: Space Physics*, *121*(7), 6378–6399. <https://doi.org/10.1002/2015ja022324>
- Poppe, A. R., Brain, D. A., Dong, Y., Xu, S., & Jarvinen, R. (2021). Particle-in-cell modeling of Martian magnetic cusps and their role in enhancing nightside ionospheric ion escape. *Geophysical Research Letters*, *48*(1), e2020GL090763. <https://doi.org/10.1029/2020gl090763>
- Ruhunusiri, S., Halekas, J. S., Espley, J. R., Eparvier, F., Brain, D., Mazelle, C., et al. (2018). An artificial neural network for inferring solar wind proxies at Mars. *Geophysical Research Letters*, *45*(2010), 855–865. <https://doi.org/10.1029/2018GL079282>
- Schwartz, S. J., Andersson, L., Xu, S., Mitchell, D. L., Akbari, H., Ergun, R. E., et al. (2019). Collisionless electron dynamics in the magnetosheath of Mars. *Geophysical Research Letters*, *46*(21), 11679–11688. <https://doi.org/10.1029/2019gl085037>
- Shane, A. D., Xu, S., Liemohn, M. W., & Mitchell, D. L. (2016). Mars nightside electrons over strong crustal fields. *Journal of Geophysical Research: Space Physics*, *121*(4), 3808–3823. <https://doi.org/10.1002/2015ja021947>
- Steckiewicz, M. (2017). *The nightside ionosphere of Mars unveiled by suprathermal electron depletions (Unpublished doctoral dissertation)*. Université Toulouse 3 Paul Sabatier (UT3 Paul Sabatier).
- Trotignon, J., Mazelle, C., Bertucci, C., & Acuna, M. (2006). Martian shock and magnetic pile-up boundary positions and shapes determined from the Phobos 2 and Mars Global Surveyor data sets. *Planetary and Space Science*, *54*(4), 357–369. <https://doi.org/10.1016/j.pss.2006.01.003>
- Xu, S., Curry, S. M., Mitchell, D. L., Luhmann, J. G., Lillis, R. J., & Dong, C. (2020). Superthermal electron deposition on the Mars nightside during ICMEs. *Journal of Geophysical Research: Space Physics*, *125*(10), e2020JA028430. <https://doi.org/10.1029/2020ja028430>
- Xu, S., Liemohn, M., Bougher, S., & Mitchell, D. (2016). Martian high-altitude photoelectrons independent of solar zenith angle. *Journal of Geophysical Research: Space Physics*, *121*(4), 3767–3780. <https://doi.org/10.1002/2015JA022149>
- Xu, S., Mitchell, D., Liemohn, M., Dong, C., Bougher, S., Fillingim, M., et al. (2016). Deep nightside photoelectron observations by MAVEN SWEA: Implications for Martian northern hemispheric magnetic topology and nightside ionosphere source. *Geophysical Research Letters*, *43*(17), 8876–8884. <https://doi.org/10.1002/2016GL070527>
- Xu, S., Mitchell, D. L., McFadden, J. P., Collinson, G., Harada, Y., Lillis, R., et al. (2018). Field-aligned potentials at Mars from MAVEN observations. *Geophysical Research Letters*, *45*(19), 10119–10127. <https://doi.org/10.1029/2018gl080136>
- Xu, S., Mitchell, D. L., McFadden, J. P., Fillingim, M. O., Andersson, L., Brain, D. A., et al. (2020). Inverted-V electron acceleration events occurring with localized auroral observations at Mars by MAVEN. *Geophysical Research Letters*, *47*(9), e2020GL087414. <https://doi.org/10.1029/2020gl087414>
- Xu, S., Schwartz, S. J., Mitchell, D. L., Horaites, K., Andersson, L., Halekas, J., et al. (2021). Cross-shock electrostatic potentials at Mars inferred from MAVEN measurements. *Journal of Geophysical Research: Space Physics*, *126*(3), e2020JA029064. <https://doi.org/10.1029/2020ja029064>
- Xu, S., Weber, T., Mitchell, D. L., Brain, D. A., Mazelle, C., DiBraccio, G. A., & Espley, J. (2019). A technique to infer magnetic topology at Mars and its application to the terminator region. *Journal of Geophysical Research: Space Physics*, *124*(3), 1823–1842. <https://doi.org/10.1029/2018ja026366>